







VECSEL systems for quantum information processing with trapped beryllium ions

S. C. BURD,^{1,2} J.-P. PENTTINEN,^{3,4} P.-Y. HOU,^{1,2}  H. M. KNAACK,^{1,2}  S. RANTA,^{3,4}  M. MÄKI,^{3,4}  E. KANTOLA,^{3,4} M. GUINA,^{3,4}  D. H. SLICHTER,¹  D. LEIBFRIED,¹ AND A. C. WILSON^{1,*}

¹Time and Frequency Division, National Institute of Standards and Technology, Boulder, Colorado 80305, USA

²Department of Physics, University of Colorado, Boulder, Colorado 80309, USA

³Optoelectronics Research Centre, Tampere University, 33720 Tampere, Finland

⁴Vexlum Ltd, Kauhakorvenkatu 53 B, 33710 Tampere, Finland

*Corresponding author: andrew.wilson@nist.gov

Received 15 September 2022; revised 18 November 2022; accepted 29 November 2022; posted 29 November 2022; published 10 March 2023

We demonstrate two systems based on vertical-external-cavity surface-emitting lasers (VECSELs) for producing ultraviolet laser light at wavelengths of 235 and 313 nm. The systems are suitable for quantum information processing with trapped beryllium ions. Each system consists of a compact, single-frequency, continuous-wave VECSEL producing high-power near-infrared light, tunable over tens of nanometers. One system generates 2.4 W at 940 nm, using a gain mirror based on GaInAs/GaAs quantum wells, which is converted to 54 mW of 235 nm light for photoionization of neutral beryllium atoms. The other system uses a gain mirror based on GaInNAs/GaAs quantum wells, enabling wavelength extension above 1200 nm with manageable strain in the GaAs lattice. This system generates 1.6 W at 1252 nm, which is converted to 41 mW of 313 nm light that is used to laser cool trapped ${}^9\text{Be}^+$ ions and quantum state preparation and detection. The 313 nm system is also suitable for implementing high-fidelity quantum gates. © 2023 Optica Publishing Group

<https://doi.org/10.1364/JOSAB.475467>

1. INTRODUCTION

Quantum information processing (QIP) technology based on atomic physics is steadily emerging from research laboratories and moving into commercial development [1]. Often the selection of the atomic system for a particular QIP application is determined more by the availability of suitable lasers than by atomic properties. This is especially apparent with atomic species requiring ultraviolet (UV) laser sources, where cost and reliability present obstacles. One important example is the beryllium ion (${}^9\text{Be}^+$), which has several properties advantageous for QIP. The low ion mass helps to achieve high secular trapping frequencies [2], allowing for faster quantum gates and ion transport operations [3,4], along with stronger Coulomb-mediated coupling between ions in separated-trap arrays [5,6]. As a result, comparable high-fidelity two-quantum bit (qubit) gates can typically be implemented with less laser intensity than is needed for heavier ion species [7]. Reducing laser requirements may be critical for scaling to larger processors [2,8–11] and eventual fault-tolerant operation. Another attractive feature of ${}^9\text{Be}^+$ ions is the ~ 1.3 GHz ground state hyperfine splitting, accessible with low-cost microwave electronics and relatively simple antennas. Qubits stored in ${}^9\text{Be}^+$ hyperfine states have exhibited coherence times of several seconds [12] and single-qubit gate errors of $2.0(2) \times 10^{-5}$ [13]. Furthermore, two-qubit gates

between ${}^9\text{Be}^+$ hyperfine qubits have been demonstrated with an error of $8(4) \times 10^{-4}$ [14], one of the lowest reported in any physical system to date.

Beryllium QIP experiments typically use laser light at 235 nm to photoionize neutral atoms, and at 313 nm for laser cooling, state preparation, quantum gates, and measurement. The relevant features of the ${}^9\text{Be}^+$ energy level structure are shown in Fig. 1. Light at 235 nm is often generated by nonlinear frequency conversion of lasers operating at 940 nm, including titanium-sapphire (Ti:S) lasers (both pulsed and CW) and semiconductor diode lasers [15]. Light at 313 nm has been generated with nonlinear frequency conversion of light from dye lasers [16], and more recently from fiber lasers [15,17] and semiconductor diode lasers [18–20]. Very recently, laser control of beryllium ions was demonstrated using a spectrally tailored optical frequency comb near 313 nm [21].

Vertical-external-cavity surface-emitting lasers (VECSELs) [22] offer a promising alternative to the approaches listed above. VECSELs combine the advantages of external-cavity solid-state disk lasers with those of quantum-well (QW) semiconductor lasers, and have made considerable progress over the last decade [23]. The external cavity geometry of these lasers enables high-power and single-frequency operation with near-diffraction-limited beam quality, in a relatively compact

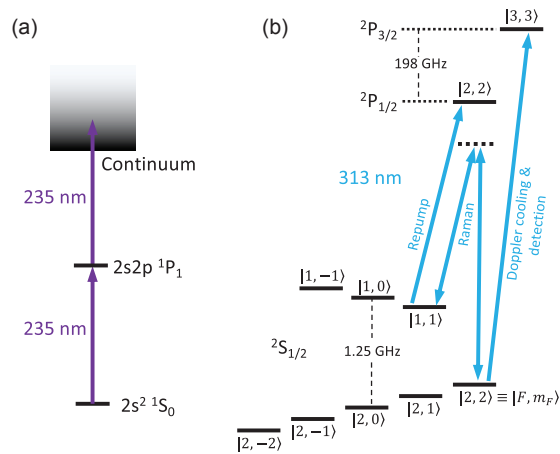


Fig. 1. Energy levels relevant to QIP with beryllium ions. (a) Energy levels of neutral ^9Be for photoionization with 235 nm light. (b) Energy levels of $^9\text{Be}^+$. Light near 313 nm is used for laser cooling, state preparation and detection, repumping, and multi-qubit quantum gates based on stimulated Raman transitions. Additional repump light resonant with $2S_{1/2}|2, 1\rangle \leftrightarrow 2P_{1/2}|2, 2\rangle$ is omitted for clarity.

package. The semiconductor gain material permits a wide tuning range and can be engineered for emission over a broad range of wavelengths. Due to the long (>10 cm) high- Q cavity and the short carrier lifetime of the semiconductor gain medium, VECSELs operate in the so-called class A regime, having cavity photon lifetimes much longer than the upper-state lifetime of the gain medium. As a result, unlike in solid-state lasers and many diode lasers, the laser dynamics are dominated by the photon lifetime in the external cavity. As a result, VECSELs produce very low-intensity-noise light [24] and do not suffer from relaxation oscillation. Owing to the large intracavity power and strong gain saturation, the broad spectral pedestal due to amplified spontaneous emission that is generally present in fiber lasers, external-cavity diode lasers, and tapered-amplifier systems is largely absent in VECSELs. These advantageous features have been validated by the demonstration of VECSEL-based systems for the generation and manipulation of trapped magnesium ions [25], with measured performance fulfilling the requirements of typical ion-trapping experiments. Although the benefits of using VECSELs in quantum-technology applications are gaining more attention (see, for example, recent publications reporting single-frequency VECSELs with sub-kHz linewidth and 140 mW single-mode output power [26], or linewidths of tens of kHz and watt-level single-mode output powers [27,28], targeting transitions in neutral Sr [26,27], neutral Cd [27], and neutral Rb [28]; a VECSEL with 22 mW single-mode output power before frequency doubling to Yb^+ ion wavelengths has also been reported [29]), single-frequency operation at wavelengths matching Be^+ ion transitions has not been demonstrated.

Here, we demonstrate two VECSEL-based systems for the generation and manipulation of trapped $^9\text{Be}^+$ ions. These systems are based on two new implementations for gain mirrors operating at fundamental wavelengths of 940 and 1252 nm, and external frequency conversion stages to generate laser light at 235 and 313 nm, respectively. The functionality of the UV lasers is assessed in terms of their ability to perform the essential

functions of ion production from neutral atoms, ion cooling, and ion state manipulation. The work demonstrates the versatility of VECSEL technology in fulfilling the needs of $^9\text{Be}^+$ and other ion systems, and its promise to provide practical solutions in a large number of quantum-technology applications.

2. LASER SYSTEMS DEVELOPMENT

A. Laser Setup

A schematic diagram of the two laser systems is shown in Fig. 2. Both VECSEL cavities consist of a specific gain mirror (i.e., designed for fundamental emission at 940 or 1252 nm) and an output-coupler (OC) mirror ($\sim 2\%$ transmission, 200 mm radius of curvature, 12.7 mm diameter) spaced approximately 125 mm apart, giving a ~ 1.2 GHz free spectral range (FSR). To provide single-frequency operation and coarse tuning, we used the following intra-cavity elements: a Brewster-angled birefringent filter (BRF, single quartz plate, 3 mm thickness) and an etalon (yttrium aluminium garnet, 1 mm thickness). Both these elements are actively temperature stabilized. For fine tuning and stabilization of the VECSEL output frequency, the small OC mirror is mounted on a ring-shaped piezo-electric transducer (PZT), which allows the cavity length to be adjusted. The gain mirror is optically pumped by a high-power, multi-mode diode laser emitting near 808 nm, which is fiber coupled and focused to produce a $\sim 200\ \mu\text{m}$ beam waist (radius) on the gain-mirror surface. Gaussian or super-Gaussian pump intensity profiles with a laser-mode-to-pump-spot ratio larger than 0.8 are typically preferred for single-mode operation [30]. Although the pump absorption band of the gain material is very broad, high-power diode lasers emitting near 808 nm were selected, as these are readily available and relatively inexpensive, and the gain mirror pump absorption length was optimized accordingly. The gain mirror copper heatsink is mounted on a thermo-electric cooler (TEC) for temperature stabilization and control. The TEC is water-cooled using a micro-channel heat exchanger and a low-vibration chiller (important for narrow-linewidth laser operation). The VECSEL cavity components are mounted on an Invar steel baseplate that is housed in an O -ring-sealed enclosure for stable operation. We have found that removing intra-cavity water vapor, by including a desiccant inside the laser enclosure and purging with dry nitrogen, improves frequency stability and output power at wavelengths where water absorption lines are present (for example, at 940 nm).

In single-mode operation of the VECSELs, coarse-range tuning (in ~ 80 GHz steps over ~ 10 THz) is achieved by BRF rotation, as well as by adjusting the BRF set-point temperature

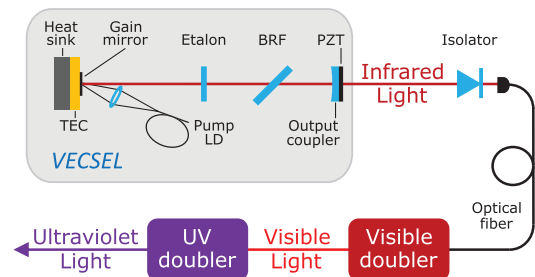


Fig. 2. Diagram of the VECSEL cavity configuration and two stages of external frequency doubling.

(0.1–1 THz range with ~ 37 GHz/K rate). Intermediate-range tuning is achieved by tilting the etalon and adjusting its temperature (1–100 GHz range with ~ 3 GHz/K rate, with ~ 1.2 GHz steps). Fine tuning is achieved by adjusting the laser cavity length using the OC PZT (0.01–1 GHz with ~ 30 MHz/V rate). By simultaneously tuning the etalon temperature and the laser cavity length, it is possible to achieve mode-hop-free tuning ranges over several GHz, limited by the maximum travel of the cavity PZT.

The VECSEL gain mirrors comprised a distributed Bragg reflector (DBR) and an active region with strain compensation layers, QWs, barrier/spacer layers, and a window layer, arranged for resonant periodic gain (RPG). Both mirrors (for 940 and 1252 nm) were fabricated using solid-source molecular beam epitaxy (MBE). A general description of VECSEL gain mirror technology and design constraints related to material systems can be found, for example, in [23,31]. Specific design details are discussed below together with the experiments on UV generation.

B. 235 nm Laser Source

The gain mirror structure for the 940 nm VECSEL is depicted with the refractive index on the left axis in Fig. 3. The positions of the cavity standing wave antinodes are important design parameters for the layer thicknesses and need to be commensurate with the simulated electric field modulus plotted on the right axis. The active region of the semiconductor multilayer structure was grown first on a GaAs substrate, followed by the GaAs/AlAs DBR. Photon emission originates from 24 GaInAs QWs in GaAs barriers that coincide with the antinodes of the standing wave, with two QWs per antinode (12×2). The choice of a relatively high number of QWs was influenced by the low bandgap offset between the barriers and the QWs, which leads to carrier leakage and poor performance of a single QW at elevated temperatures. In fact, the carrier confinement is the main mechanism limiting the minimum wavelength of the GaInAs/GaAs material system [32]. For comparison, we note that a typical gain structure enabling high-power operation at $> 1 \mu\text{m}$ consists of 10 to 12 QWs placed as one QW per antinode [33]. The active region also includes GaAsP strain compensation layers.

For proper VECSEL operation, the heat resulting from pump laser absorption must be removed and the temperature of the gain mirror must be stabilized. To this end, for the 940 nm gain mirror we used a standard flip-chip cooling method [22] where the heat flows from the active region through the DBR

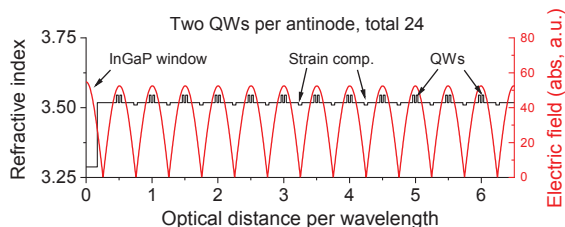


Fig. 3. Schematic active region design for the 940 nm gain mirror with a total of 24 quantum wells (QWs), depicted with refractive index (black, on left axis) and simulated cavity standing-wave electric field modulus (red, on right axis) for reference.

to the heat spreader. For this purpose, the as-grown gain mirror was first diced into $2.5 \times 2.5 \text{ mm}^2$ chips and the DBR back surface of each chip was bonded to a $3 \times 3 \times 0.3 \text{ mm}^3$ synthetic multi-crystal diamond heat spreader. After bonding, the GaAs substrate was removed with a combination of mechanical lapping and wet etching. An ion-beam-sputtered (IBS) anti-reflection (AR) coating was applied to the top surface of the approximately $5\text{-}\mu\text{m}$ -thick semiconductor structure for reduced reflection of pump and laser light and for protection of the gain chip surface. Finally, the diamond back surface was soldered to a temperature-stabilized copper heat sink for efficient heat extraction.

Performance characteristics of the 940 nm VECSEL are shown in Fig. 4. With 14.5 W of pump power, the tuning range is ~ 30 nm, and the slope efficiency at 940 nm is 27(1)% for single-frequency operation. To estimate the VECSEL linewidth, we analyze the beat note signal between the 940 nm VECSEL output and that of a free-running TiS laser (nominal linewidth < 50 kHz), with the VECSEL frequency-offset locked to the TiS laser [34]. From the spectral width of the beat signal, we determine the linewidth of the VECSEL to be < 100 kHz. This is considerably less than the linewidth of relevant atomic transitions and sufficiently narrow that frequency fluctuations will not be converted to significant amplitude fluctuations by subsequent resonant frequency-doubling stages.

The output of the 940 nm VECSEL is coupled into a high-power polarization-maintaining (PM) optical fiber that delivers light to the first of two second-harmonic generation (SHG) enhancement cavities. This 940–470 nm frequency-doubling cavity is locked to the single-frequency output of the VECSEL using the Pound–Drever–Hall (PDH) method [35], with the sidebands generated via electro-optic modulation of infrared

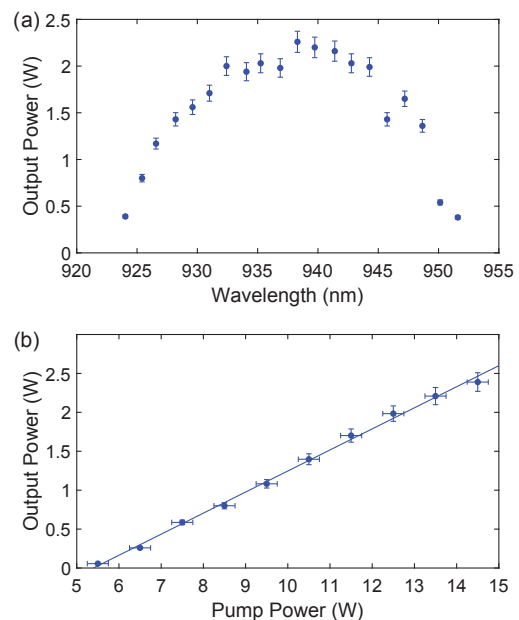


Fig. 4. (a) Single-mode output power at 940 nm as a function of wavelength with 14.5 W pump power, obtained by rotating the BRF and tuning etalon temperature at each wavelength. (b) Output power at 940 nm versus 808 nm pump power. A linear fit to the data (solid line) gives a slope efficiency of 27(1)%. Power measurement uncertainty is 5%, and the wavelength accuracy uncertainty is 0.002 nm.

light. Following the design by Lo and colleagues [15], frequency doubling to 470 nm is implemented using a periodically poled potassium titanyl phosphate (PPKTP) nonlinear optical crystal (Raicol Crystals, 20 mm length [36]). The performance of the VECSEL-driven 470 nm source is shown in Fig. 5(a). With 0.48(2) W at 940 nm, we obtain 0.27(1) W at 470 nm. While this is more than sufficient for our application, we note that the 940 nm power to the doubling cavity could be further increased. However, cavity-locking instabilities due to apparent thermal lensing in the crystal prevent reliable locking above ~ 0.50 W at 940 nm [15,37].

The second stage of frequency doubling, from 470 to 235 nm, is implemented using an enhancement cavity design [15], adapted from an earlier 313 nm design [17], that uses a Brewster-angled beta barium borate (BBO) crystal. This doubling cavity is locked using the technique developed by Hansch and Couillaud [38]. The performance of the 235 nm frequency-doubling stage is shown in Fig. 5(b). With 0.27(1) W at 470 nm, we obtain 54(3) mW at 235 nm, and a maximum power ratio of approximately 20%. For context, this UV power is approximately 50 times greater than the power we typically use to photoionize beryllium atoms to load them into an ion trap.

C. 313 nm Laser Source

The design strategy of the 1252 nm gain chip follows different considerations. First, to increase the operation wavelength, we use GaInNAs/GaAs QWs. Without nitrogen, the high indium content required to reach emission at 1252 nm would deteriorate the crystal quality due to the high cumulative strain caused by the large lattice mismatch between the QWs and the GaAs

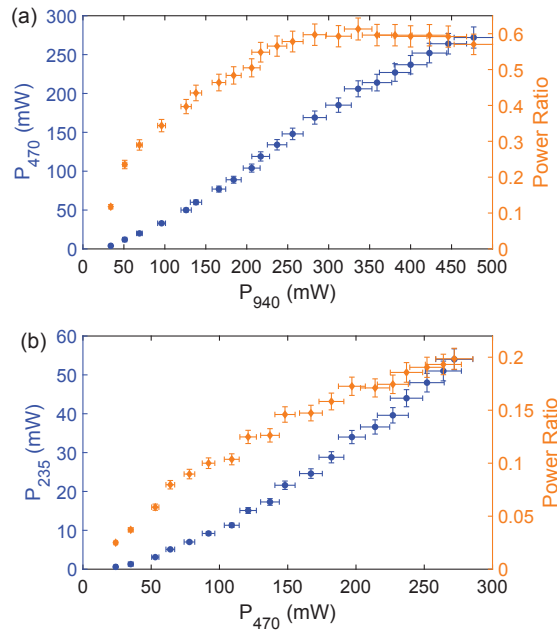


Fig. 5. Measured output powers and efficiencies of frequency-doubling stages used in the 940 nm VECSEL system. (a) 470 nm power (blue circles) and 470–940 nm power ratio (orange diamonds), versus input power at 940 nm. (b) 235 nm power (blue circles) and 235–470 nm power ratio (orange diamonds) versus input power at 470 nm. Uncertainty in all power measurements is 5%.

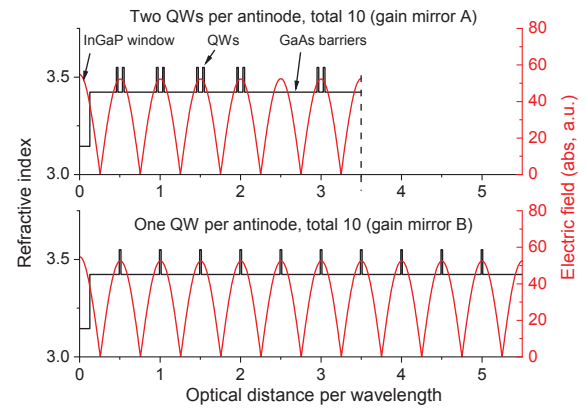


Fig. 6. Schematic active region designs for the 1.25 μm gain mirrors A and B, depicted with refractive index (black, on left axis) and simulated cavity standing-wave electric field modulus (red, on right axis) for reference.

barriers. In fact, the strain is the main limiting mechanism for the upper wavelength of the GaInAs/GaAs system [23]. The use of a small percentage of N enables us to achieve a certain bandgap at significantly smaller In content due to bandgap bowing [39]. At the same time, the lattice constant decreases, reducing the lattice mismatch to GaAs. Another positive effect is that N affects only the conduction band, and therefore, for a certain bandgap, a GaInNAs/GaAs QW would offer higher conduction-band offset compared to a GaInAs/GaAs QW. This has a positive effect on carrier capture ability and temperature behavior, the opposite of the effect we mentioned as being detrimental for the 940 nm QWs. However, growing GaInNAs materials is technically challenging owing to N -related induced defects, which become more detrimental as the N content is increased to achieve longer-wavelength operation [40]. The best compromise between detrimental effects from N -related defects and strain management is to minimize the amount of N to a level just sufficient to avoid structural strain-related dislocations. One should also employ efficient pumping of N from the MBE chamber after the growth of QWs. To this end, immediately after the growth of QWs, the N -plasma source is isolated by a gate valve, and an ion pump is activated for fast pumping of residual N . This procedure helps us avoid the formation of N -related defects that can induce nonradiative recombination in the barrier regions. We also optimize overall thickness of the barrier region, i.e., the total thickness of the GaAs absorbing layers in between the QWs, so that sufficient pump power is available through the entire structure to achieve the required carrier density in the QWs closest to the DBR. In this way, we have fabricated two gain mirror structures for operation near 1250 nm, schematically shown in Fig. 6.

Both structures contain 10 GaInNAs QWs surrounded by GaAs barriers, without strain-compensating GaAsP or GaAsN layers. In structure A, the QWs were distributed two per antinode in the first six antinodes, the last pair having a thicker pumping region around it, while in structure B, the QWs were distributed according to the conventional design [33], one per antinode, which should lead to a smaller threshold owing to better superposition of the QWs with the optical field antinodes. The main rationale for assessing design A in

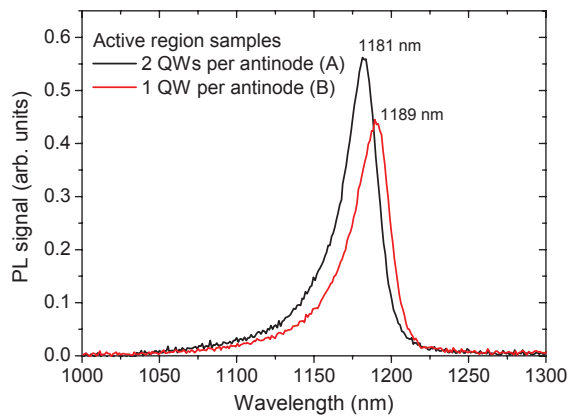


Fig. 7. Photoluminescence (PL) spectra of the 1.25 μm VECSEL gain mirror calibration samples for structures A (black) and B (red) under 785 nm excitation.

addition to the more conventional design B was to minimize the interfaces between N -containing material and the GaAs barrier regions grown without N background, and thus to minimize the overall defect density. We also wanted to experiment with the physical thickness of the structure, which affects the pump absorption. The pump absorption efficiency was estimated using the absorption coefficient 13900 cm^{-1} [41] for GaAs and the exponential decay of pump intensity. The active region thicknesses were $\sim 1200\text{ nm}$ and $\sim 1900\text{ nm}$ for gain mirrors A and B, respectively, while the active region thickness for the 940 nm structure above was $\sim 1600\text{ nm}$ for reference. These absorption thicknesses correspond roughly to 81% (gain mirror A) and 93% (gain mirror B) single-pass pump absorption efficiencies, and 89% for the 940 nm gain mirror.

The GaInNAs QWs were grown at a temperature of $\sim 475^\circ\text{C}$ (thermocouple set point); this relatively low temperature compared to the growth of GaInAs QWs (in the range of 650°C) is required to avoid N -related phase separation. The As/III beam equivalent pressure (BEP) ratio was 14 for both structures. The estimated nominal QW compositions were $\text{GaIn}_{0.31}\text{N}_{0.07}\text{As}$ and $\text{GaIn}_{0.31}\text{N}_{0.05}\text{As}$ for gain mirrors A and B, respectively. The N -plasma parameters were the same for both structures, and the composition difference resulted from variation in the growth rate ($\sim 1\text{ }\mu\text{m/h}$ for structure A and $\sim 1.3\text{ }\mu\text{m/h}$ for structure B). The photoluminescence (PL) spectra of QW calibration samples (i.e., without DBRs) are shown in Fig. 7. The room-temperature PL peak wavelengths for the two structures were 1181 nm (gain mirror A) and 1189 nm (gain mirror B). The active region of the gain mirror B emitted at a slightly longer wavelength despite the lower nominal N composition. Most likely this was due to inaccuracy in the In and/or Ga growth rate calibration or flux measurement. Nevertheless, both structures showed strong and narrow (FWHM 27–29 nm) PL peaks under 785 nm excitation. Under strong optical pumping resulting in heating, the emission of the QWs typically shifts to the red by $\sim 10\text{ THz}$ (corresponding to $\sim 50\text{ nm}$ shift near $\sim 1200\text{ nm}$).

For the 1252 nm gain mirrors, we used a so-called top emitting cooling configuration that is better suited for devices operating at longer wavelengths. The gain mirrors were first diced into $3 \times 3\text{ mm}^2$ chips, and the active-region surface of each was liquid-capillary bonded to a transparent heat spreader.

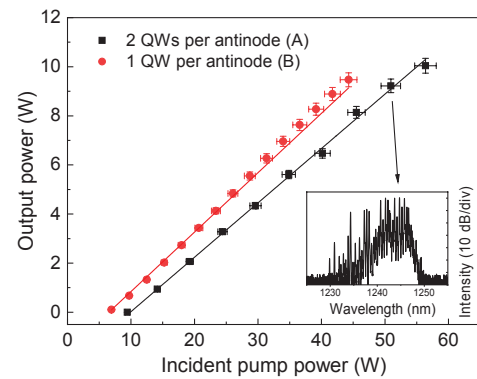


Fig. 8. Multimode power characteristics for the 1252 nm VECSEL gain mirror structures A (black squares) and B (red spheres). The mount temperature was set to 18°C . Uncertainty of power measurement at each data point is 3%.

The advantage of this so-called intra-cavity cooling configuration is that the low-thermal-conductivity DBR is not in the heat path between the hot active region and the heat spreader. However, since the intra-cavity beam passes through the heat spreader in this configuration, it has to be of good optical quality. We used a $3 \times 3 \times 0.25\text{ mm}^3$ synthetic single-crystal diamond heat spreader, polished with a 2° angle between facets to suppress spurious etalons. The top surface of the diamond was soldered to a copper heatsink with an opening for the intra-cavity beam to access the gain mirror. Finally, the diamond top surface was AR-coated (using IBS) to minimize intra-cavity loss and etaloning. For the 940 nm gain mirrors, we tested only flip-chip devices, which are often preferred because multi-crystal diamond heat spreaders are more easily sourced and lower cost than single-crystal ones.

The different gain mirrors were first tested in a multi-mode configuration for rough assessment of their output power and wavelength capability. For this, we used a V-shaped cavity with a high-reflectivity folding mirror with 75 mm radius of curvature, and flat output coupling mirror with 1% transmittance, with cavity arm lengths of 72 and 50 mm as measured from the gain mirror. The simulated fundamental mode diameter on the gain mirror was $260\text{ }\mu\text{m}$ (tangential) and $300\text{ }\mu\text{m}$ (sagittal), and the 808 nm pump laser spot diameter was $\sim 400\text{ }\mu\text{m}$, incident at a 30° angle from the gain chip surface normal. Gain mirrors A (two QWs per antinode) and B (one QW per antinode) had lasing threshold pump powers of 9.6 and 6.9 W, respectively (see Fig. 8). The multi-mode output powers with 40 W incident pump power were 6.7 W (A, with optical to optical power conversion efficiency of 17%) and 8.5 W (B, 21%), and the lasing central wavelengths at 9 W of output power were 1245 nm (A) and 1230 nm (B). Although structure B showed a smaller threshold and higher slope efficiency, structure A was selected for the final single-frequency VECSEL assembly, as it exhibited free-running emission wavelengths closer to the 1252 nm target wavelength. As described below, the 1252 nm VECSEL delivers nearly twice the single-frequency output power at 1231 nm than at the target wavelength of 1252 nm, suggesting room for future improvement.

Initial characterization of the assembled 1252 nm VECSEL was performed by measuring the output power and wavelength

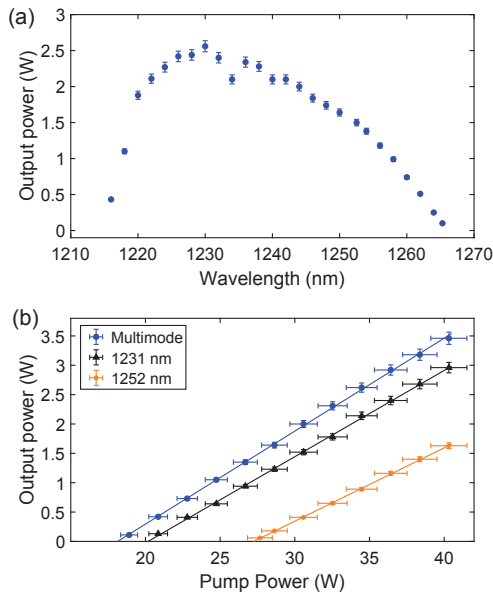


Fig. 9. (a) Output power of the 1252 nm VECSEL as a function of wavelength in single-frequency operation at 40.3 W pump power, obtained by rotating the BRF and adjusting the etalon and gain chip temperatures at each wavelength to optimize the output power. (b) Measured VECSEL output powers, under three different operating conditions, versus the input power of the 808 nm pump laser. Solid lines are linear fits used to determine slope efficiencies. Uncertainty of power measurement at each data point in (a) and (b) is 3%.

tuning range of the laser (Fig. 9). In multi-longitudinal mode operation (with BRF and etalon removed), a maximum output power of 3.5(1) W at 1231 nm and a slope efficiency of 15.8(3)% were measured [Fig. 9(b)]. In single-frequency operation (with BRF and etalon installed), we measured a reduced slope efficiency of 14.7(3)% and an output up to 3.0(1) W at 1231 nm due to the additional loss from the intra-cavity elements. When tuned to the target wavelength for our application (1252 nm), a slope efficiency of 12.5(2)% and output up to 1.63(5) W were obtained. The VECSEL was tunable over a 50 nm range. The tuning range was limited at shorter wavelengths by the available gain chip cooling power. We note that roll-over in the output power at the highest pump power was not observed, suggesting that higher output power could be achieved by increasing the pump power. We anticipate fabricating future gain mirrors with peak gain closer to the target wavelength by optimizing the active region thickness and the QW number and composition.

For conversion of 1252 nm light to 626 nm, a commercial, fiber-coupled, periodically poled lithium-niobate waveguide doubler (NTT Electronics Corp, model WH-0626-000-A-B-C [36]) is used. The temperature of the waveguide is controlled by a TEC to maintain the quasi-phase matching condition. For this conversion stage, with 1.63(5) W of 1252 nm power from the VECSEL, we obtain a maximum power of 0.53(3) W at 626 nm and a power ratio of 33(2)% (including loss from the fiber coupling into the waveguide). The maximum power at 626 nm is limited by the available 1252 nm power. We note that 2.4 W at 671 nm has been generated using a similar waveguide-based SHG device [42].

The 626 nm light from the waveguide doubler is coupled into a PM optical fiber and delivered to a cavity-enhanced SHG setup [17] that uses a Brewster-angled BBO crystal for conversion to 313 nm. With 0.33(2) W input power, we obtain 41(2) mW at 313 nm.

To estimate the spectral linewidth of the 1252 nm VECSEL, we analyze the beat note signal between the 626 nm output of the waveguide doubler and the output of a frequency-stabilized fiber-laser-based 626 nm source similar to that described in [17]. Following the approach described above for the analysis of the 940 nm VECSEL, the 1252 nm VECSEL is frequency-offset-locked to the fiber-laser source [34]. From the spectral width of the beat signal, we estimate the linewidth of the 1252 nm VECSEL to be <110 kHz. This is also considerably less than the linewidths of relevant atomic transitions and sufficiently narrow that frequency fluctuations will not be converted to significant amplitude fluctuations by the resonant UV frequency-doubling stage.

3. TESTS WITH BERYLLIUM ATOMS AND IONS

The VECSEL systems were tested with neutral ^9Be and $^9\text{Be}^+$ ions in two different experimental setups.

Photoionization with the 235 nm VECSEL system was tested on a thermal beam of neutral beryllium atoms. The thermal beam was generated by resistively heating a length of beryllium wire spiral-wound onto tungsten support wire. The beam was weakly collimated using a 2.5 mm diameter aperture. Immediately downstream from the aperture, the atomic beam intersected with a perpendicular 235 nm laser beam near-resonant with the 1S_0 to 1P_1 transition and focused to an intensity of $\sim 80(20)$ kW/m² at the center of the atomic beam. For comparison, the saturation intensity of this transition is ~ 8.7 kW/m² [43]. Ions are produced by a two-photon process [see Fig. 1(a)]. On resonance, the first photon excites the neutral atom to the 1P_1 state, and a second photon excites the electron to the continuum. These ions are counted using a Channeltron electron multiplier (CEM) (Photonis Magnum 5901 Electron Multiplier [36]) with a bias potential of -1.7 kV.

With the neutral atomic beam flux held constant, we record the ion count rate as a function of VECSEL frequency to obtain a photoionization line shape (Fig. 10). Maximum photoionization rates are measured at a VECSEL frequency of 319.0200(6) THz, corresponding to 1276.080(2) THz in the UV, consistent with a recent precision measurement of the 1S_0 to 1P_1 transition [43]. The central feature of the photoionization line shape includes contributions from the natural linewidth of 87(5) MHz [43], power broadening by a factor of $\sim 2.4(3)$, and 1.3(2) GHz of residual Doppler broadening from imperfect collimation of the atomic beam [44]. A Voigt model [44] including only these mechanisms shows good agreement with the central feature. The origin of the weak off-resonant photoionization (the broad pedestal feature of the line shape) has not been investigated.

The 313 nm laser source was used to perform Doppler cooling, resonant detection, and repumping in an established trapped-ion system described in [45]. For convenience, we locked the frequency of the 626 nm light produced by the frequency-doubled VECSEL to 626 nm light produced by

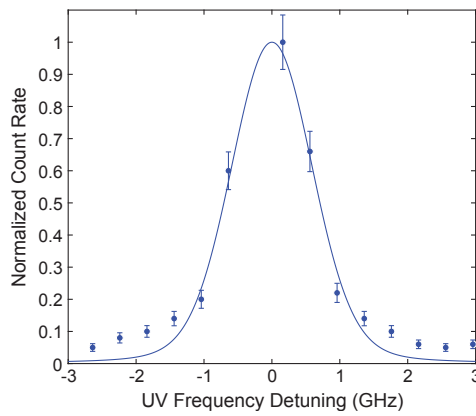


Fig. 10. Count rate measured by the CEM as a function of the quadrupled VECSEL (UV) frequency detuning from 1276.080(2) THz. The central peak is overlaid with a Voigt model. Count rate measurement uncertainty is estimated to be 4%.

an existing fiber laser system used for ${}^9\text{Be}^+$ ion trapping [17] that is frequency referenced to a molecular iodine absorption line. We used the 313 nm laser source for Doppler cooling single ${}^9\text{Be}^+$ ions loaded in the trap. The frequency-quadrupled light at 313 nm was polarized σ^+ and then tuned across the ${}^2S_{1/2}|2, 2\rangle \leftrightarrow {}^2P_{3/2}|3, 3\rangle$ cycling transition at approximately 957.397 THz using an acousto-optic modulator (AOM). Fluorescence photons were collected by an optical imaging system and counted using a photo-multiplier tube (PMT). The resulting spectrum is shown in Fig. 11(a). Within laser-intensity uncertainties, the line shape obtained with the VECSEL source is identical to that obtained with our fiber laser source.

To test optical pumping with the VECSEL source, the σ^+ polarized laser is tuned into resonance with the ${}^2S_{1/2} \leftrightarrow {}^2P_{1/2}$ transition of ${}^9\text{Be}^+$ at approximately 957.200 THz [Fig. 1(b)]. We swept the frequency across the atomic transition using an AOM and then fixed the frequency to resonance. Then a single ${}^9\text{Be}^+$ ion was prepared in the $|1, 1\rangle$ state by first optically pumping to the $|2, 2\rangle$ state using a second (fiber laser generated) light field near 313 nm and then applying a microwave π pulse resonant with the $|2, 2\rangle \leftrightarrow |1, 1\rangle$ transition. Repumping light generated by the VECSEL system is then applied for various durations, ideally repumping the ion to the $|2, 2\rangle$ state for subsequent fluorescence detection with light resonant with the ${}^2S_{1/2}|2, 2\rangle \leftrightarrow {}^2P_{3/2}|3, 3\rangle$ cycling transition generated by the second system [see Fig. 1(b)]. The detection in each experiment yields a binary outcome; the ion either fluoresces significantly or it does not. By setting a threshold of 10 counts, we can reliably assign a zero or one to the outcome of a given experiment. For each duration, the population of $|2, 2\rangle$ is determined by calculating the mean of the results from 300 experimental repetitions. The repump time $\tau = 0.55(4) \mu\text{s}$ is determined by fitting the exponential function $1 - e^{-t/\tau}$, where t is the repumping pulse duration, to the data in Fig. 11(b). Accounting for laser-intensity differences, the repumping obtained using the VECSEL system is indistinguishable from that obtained with our fiber laser source.

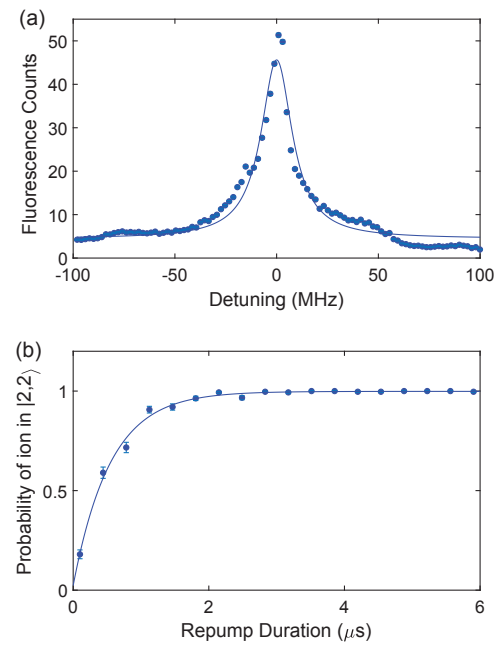


Fig. 11. (a) Spectroscopy of the ${}^2S_{1/2}|2, 2\rangle \leftrightarrow {}^2P_{3/2}|3, 3\rangle$ cycling transition with UV light from the 313 nm VECSEL source. Each data point indicates the mean of 300 experimental repetitions, each with a 330 μs detection period. The solid line is a Lorentzian fit to the data, and the detuning is with respect to the center of the fitted line. (b) Probability of measuring ${}^2S_{1/2}|2, 2\rangle$ after repumping from the ${}^2S_{1/2}|1, 1\rangle$ state with UV light from the 313 nm VECSEL source. The solid curve is an exponential fit. Data points indicate the mean of 300 repetitions. Error bars in (a) and (b) indicate the standard deviation of the mean.

4. CONCLUSION

In summary, we have presented two widely tunable VECSEL-based laser sources capable of implementing tasks for QIP experiments involving trapped ${}^9\text{Be}^+$ ions. The first system generated up to 2.4 W single-frequency light at 940 nm and was frequency doubled twice to generate 235 nm light for photoionization of neutral Be. Over more than eight months of continuous use at an output power of about 1 W, we observe long-term power drifts at 940 nm of less than 10%. The frequency of the VECSEL is locked to a wavemeter. We distribute the 470 nm light from the same VECSEL to multiple UV doublers used for different trapped-ion setups; each doubler produces a few mW at 235 nm, sufficient for producing ${}^9\text{Be}^+$ ions in our experiments. The second system produced up to 1.6 W at 1252 nm, which was converted to 313 nm by two stages of frequency doubling, and can be used for Doppler cooling, detection, and repumping of trapped ${}^9\text{Be}^+$ ions. We note that the large tuning range of the 940 nm VECSEL system presented in this work could allow for generation of light near 313 nm by third-harmonic generation [20]. The inherent power scalability of the VECSEL design should allow the generation of higher output power [22], which is desirable for mitigating spontaneous emission errors associated with quantum-logic gates using far-detuned stimulated Raman transitions [7]. Further improvements to overall system efficiency could be achieved using intra-cavity SHG [46].

The VECSEL platform presents improved size, weight, and power, and cost (SWaP-C) performance compared to established tunable high-power laser solutions based on Ti:S lasers. This can be simply understood given the fact that Ti:S gain media are commonly pumped with single-mode green lasers, which by themselves have size comparable to a VECSEL. Indeed, many such pump lasers are in fact intracavity-frequency-doubled VECSELs. While the VECSELs reported here are laboratory prototypes, they exhibit good prospects for miniaturization, with current developments focused on creating much smaller modules with intracavity doubling and integrated pump laser diodes. Ultimately, the size of the system will be limited by the control electronics including frequency locking. Simplifications in direct VECSEL systems over Ti:S could translate into lower cost.

Funding. National Institute of Standards and Technology (Quantum Information Program); Academy of Finland (project QUBIT (278388)).

Acknowledgment. S.C.B., J.-P.P., P.-Y.H., and H.M.K. all contributed equally to this work. We thank Stephen Erickson, Jenny Wu, Daniel Cole, and Yong Wan for assistance in the laboratory, and Richard Fox and Jenny Wu for comments on the manuscript. P.-Y.H., H.M.K., and S.C.B. acknowledge support of the Professional Research Experience Program (PREP), operated jointly by NIST and the University of Colorado. J.-P.P. acknowledges support of the Jenny and Antti Wihuri Foundation, the Walter Ahlström Foundation, and the Finnish Foundation for Technology Promotion. Vexlum Ltd. provided the gain chips for both systems described in this paper.

Disclosures. M. G.: Vexlum Ltd. (I, E), E. K.: Vexlum Ltd. (I, E), M. M.: Vexlum Ltd. (I, E), J.-P. P.: Vexlum Ltd. (I, E), S. R.: Vexlum Ltd. (I, E).

Data availability. Data underlying the results presented in this paper are not publicly available at this time but may be obtained from the authors upon reasonable request.

REFERENCES AND NOTES

- C. D. Bruzewicz, J. Chiaverini, R. McConnell, and J. M. Sage, "Trapped-ion quantum computing: progress and challenges," *Appl. Phys. Rev.* **6**, 021314 (2019).
- D. J. Wineland, C. Monroe, W. M. Itano, D. Leibfried, B. E. King, and D. M. Meekhof, "Experimental issues in coherent quantum-state manipulation of trapped atomic ions," *J. Res. Nat. Inst. Stand. Technol.* **103**, 259 (1998).
- R. Bowler, J. Gaebler, Y. Lin, T. R. Tan, D. Hanneke, J. D. Jost, J. P. Home, D. Leibfried, and D. J. Wineland, "Coherent diabatic ion transport and separation in a multizone trap array," *Phys. Rev. Lett.* **109**, 080502 (2012).
- A. Walther, F. Ziesel, T. Ruster, S. T. Dawkins, K. Ott, M. Hettrich, K. Singer, F. Schmidt-Kaler, and U. Poschinger, "Controlling fast transport of cold trapped ions," *Phys. Rev. Lett.* **109**, 080501 (2012).
- A. C. Wilson, Y. Colombe, K. R. Brown, E. Knill, D. Leibfried, and D. J. Wineland, "Tunable spin-spin interactions and entanglement of ions in separate potential wells," *Nature* **512**, 57–60 (2014).
- K. R. Brown, C. Ospelkaus, Y. Colombe, A. C. Wilson, D. Leibfried, and D. J. Wineland, "Coupled quantized mechanical oscillators," *Nature* **471**, 196–199 (2011).
- R. Ozeri, W. M. Itano, R. B. Blakestad, J. Britton, J. Chiaverini, J. D. Jost, C. Langer, D. Leibfried, R. Reichle, S. Seidelin, J. H. Wesenberg, and D. J. Wineland, "Errors in trapped-ion quantum gates due to spontaneous photon scattering," *Phys. Rev. A* **75**, 042329 (2007).
- A. M. Steane, "How to build a 300 bit, 1 giga-operation quantum computer," *Quantum Inf. Comput.* **7**, 171 (2004).
- D. Kielpinski, C. Monroe, and D. J. Wineland, "Architecture for a large-scale ion-trap quantum computer," *Nature* **417**, 709–711 (2002).
- C. Monroe and J. Kim, "Scaling the ion trap quantum processor," *Science* **339**, 1164–1169 (2013).
- K. K. Mehta, C. D. Bruzewicz, R. McConnell, R. J. Ram, J. M. Sage, and J. Chiaverini, "Integrated optical addressing of an ion qubit," *Nat. Nanotechnol.* **11**, 1066–1070 (2016).
- C. Langer, R. Ozeri, J. D. Jost, J. Chiaverini, B. DeMarco, A. Ben-Kish, R. B. Blakestad, J. Britton, D. B. Hume, W. M. Itano, D. Leibfried, R. Reichle, T. Rosenband, T. Schaetz, P. O. Schmidt, and D. J. Wineland, "Long-lived qubit memory using atomic ions," *Phys. Rev. Lett.* **95**, 060502 (2005).
- K. R. Brown, A. C. Wilson, Y. Colombe, C. Ospelkaus, A. M. Meier, E. Knill, D. Leibfried, and D. J. Wineland, "Single-qubit-gate error below 10^{-4} in a trapped ion," *Phys. Rev. A* **84**, 030303 (2011).
- J. P. Gaebler, T. R. Tan, Y. Lin, Y. Wan, R. Bowler, A. C. Keith, S. Glancy, K. Coakley, E. Knill, D. Leibfried, and D. J. Wineland, "High-fidelity universal gate set for $^9\text{Be}^+$ ion qubits," *Phys. Rev. Lett.* **117**, 060505 (2016).
- H.-Y. Lo, J. Alonso, D. Kienzler, B. C. Keitch, L. E. de Clercq, V. Negnevitsky, and J. P. Home, "All-solid-state continuous-wave laser systems for ionization, cooling and quantum state manipulation of beryllium ions," *Appl. Phys. B* **114**, 17–25 (2014).
- L. R. Brewer, J. D. Prestage, J. J. Bollinger, W. M. Itano, D. J. Larson, and D. J. Wineland, "Static properties of a non-neutral $^9\text{Be}^+$ -ion plasma," *Phys. Rev. A* **38**, 859 (1988).
- A. C. Wilson, C. Ospelkaus, A. P. VanDevender, J. A. Mlynek, K. R. Brown, D. Leibfried, and D. J. Wineland, "A 750-mW, continuous-wave, solid-state laser source at 313 nm for cooling and manipulating trapped $^9\text{Be}^+$ ions," *Appl. Phys. B* **105**, 741–748 (2011).
- H. Ball, M. Lee, S. Gensemer, and M. Biercuk, "A high-power 626 nm diode laser system for beryllium ion trapping," *Rev. Sci. Instrum.* **84**, 063107 (2013).
- F. Cozijn, J. Biesheuvel, A. Flores, W. Ubachs, G. Blume, A. Wicht, K. Paschke, G. Erbert, and J. Koelemeij, "Laser cooling of beryllium ions using a frequency-doubled 626 nm diode laser," *Opt. Lett.* **38**, 2370–2372 (2013).
- R. A. Carollo, D. A. Lane, E. K. Kleiner, P. A. Kyaw, C. C. Teng, C. Y. Ou, S. Qiao, and D. Hanneke, "Third-harmonic-generation of a diode laser for quantum control of beryllium ions," *Opt. Express* **25**, 7220–7229 (2017).
- A.-G. Paschke, G. Zanonello, H. Hahn, T. Lang, C. Manzoni, M. Marangoni, G. Cerullo, U. Morgner, and C. Ospelkaus, "Versatile control of Be^+ 9 ions using a spectrally tailored UV frequency comb," *Phys. Rev. Lett.* **122**, 123606 (2019).
- M. Kuznetsov, F. Hakimi, R. Sprague, and A. Mooradian, "High-power ($>0.5\text{-W}$ CW) diode-pumped vertical-external-cavity surface-emitting semiconductor lasers with circular TEM/sub 00/beams," *IEEE Photon. Technol. Lett.* **9**, 1063 (1997).
- M. Guina, A. Rantamäki, and A. Härkönen, "Optically pumped VECSELs: review of technology and progress," *J. Phys. D* **50**, 383001 (2017).
- M. Myara, M. Sellahi, A. Laurain, A. Michon, I. Sagnes, and A. Garnache, "Noise properties of NIR and MIR VECSELs," *Proc. SPIE* **8606**, 86060Q (2013).
- S. C. Burd, D. T. Allcock, T. Leinonen, J.-P. Penttinen, D. H. Slichter, R. Srinivas, A. C. Wilson, R. Jördens, M. Guina, D. Leibfried, and D. J. Wineland, "VECSEL systems for the generation and manipulation of trapped magnesium ions," *Optica* **3**, 1294–1299 (2016).
- P. H. Moriya, R. Casula, G. A. Chappell, D. C. Parrotta, S. Ranta, H. Kahle, M. Guina, and J. E. Hastie, "InGaN-diode-pumped AlGaInP VECSEL with sub-kHz linewidth at 689 nm," *Opt. Express* **29**, 3258–3268 (2021).
- J. N. Tinsley, S. Bandrupally, J.-P. Penttinen, S. Manzoor, S. Ranta, L. Salvi, M. Guina, and N. Poli, "Watt-level blue light for precision spectroscopy, laser cooling and trapping of strontium and cadmium atoms," *Opt. Express* **29**, 25462–25476 (2021).
- J. C. Hill, W. K. Holland, P. D. Kunz, K. C. Cox, J.-P. Penttinen, E. Kantola, and D. H. Meyer, "Intra-cavity frequency-doubled VECSEL system for narrow linewidth Rydberg EIT spectroscopy," *Opt. Express* **30**, 41408–41421 (2022).
- J. R. C. Woods, H. Kahle, A. C. Gray, J. Daykin, A. C. Tropper, C. Gawith, M. Guina, and V. Apostolopoulos, "High power 739 nm VECSELs for future Yb+ ion cooling," *Appl. Opt.* **60**, 676–680 (2021).

30. A. Laurain, J. Hader, and J. V. Moloney, "Modeling and optimization of transverse modes in vertical-external-cavity surface-emitting lasers," *J. Opt. Soc. Am. B* **36**, 847–854 (2019).
31. A. Tropper and S. Hoogland, "Extended cavity surface-emitting semiconductor lasers," *Prog. Quantum. Electron.* **30**, 1–43 (2006).
32. J. Chilla, Q.-Z. Shu, H. Zhou, E. Weiss, M. Reed, and L. Spinelli, "Recent advances in optically pumped semiconductor lasers," *Proc. SPIE* **6451**, 645109 (2007).
33. B. Heinen, M. Sparenberg, A. Weber, B. Kunert, J. Hader, S. Koch, J. Moloney, M. Koch, and W. Stolz, "106 W continuous-wave output power from vertical-external-cavity surface-emitting laser," *Electron. Lett.* **48**, 516–571 (2012).
34. A. Castrillo, E. Fasci, G. Galzerano, G. Casa, P. Laporta, and L. Gianfrani, "Offset-frequency locking of extended-cavity diode lasers for precision spectroscopy of water at 1.38 μm ," *Opt. Express* **18**, 21851–21860 (2010).
35. R. Drever, J. Hall, F. Kowalski, J. Hough, G. Ford, A. Munley, and H. Ward, "Laser phase and frequency stabilization using an optical resonator," *Appl. Phys. B* **31**, 97–105 (1983).
36. Certain commercial equipment and materials are identified in this paper in order to specify the experimental procedure accurately. Such identification does not imply recommendation or endorsement by the National Institute of Standards and Technology, nor does it imply that the equipment or materials identified are necessarily the best available for the purpose.
37. R. Le Targat, J.-J. Zondy, and P. Lemonde, "75%-efficiency blue generation from an intracavity PPKTP frequency doubler," *Opt. Commun.* **247**, 471–481 (2005).
38. T. Hansch and B. Couillaud, "Laser frequency stabilization by polarization spectroscopy of a reflecting reference cavity," *Opt. Commun.* **35**, 441–444 (1980).
39. I. Vurgaftman and J. R. Meyer, "Band parameters for nitrogen-containing semiconductors," *J. Appl. Phys.* **94**, 3675–3696 (2003).
40. K. Ville-Markus, "High-power dilute nitride lasers grown by molecular beam epitaxy," Ph.D. thesis (Tampere University of Technology, 2015).
41. M. D. Sturge, "Optical absorption of gallium arsenide between 0.6 and 2.75 eV," *Phys. Rev.* **127**, 768–773 (1962).
42. N. Kretzschmar, U. Eismann, F. Sievers, F. Chevy, and C. Salomon, "2.4-watts second-harmonic generation in ppZnO: LN ridge waveguide for lithium laser cooling," *Opt. Express* **25**, 14840–14855 (2017).
43. E. C. Cook, A. D. Vira, C. Patterson, E. Livernois, and W. D. Williams, "Testing quantum electrodynamics in the lowest singlet state of neutral beryllium-9," *Phys. Rev. Lett.* **121**, 053001 (2018).
44. W. Demtröder, *Spectroscopic Instrumentation* (Springer, 1981).
45. T. R. Tan, "High-fidelity entangling gates with trapped-ions," Ph.D. thesis (University of Colorado at Boulder, 2016).
46. E. Kantola, T. Leinonen, S. Ranta, M. Tavast, and M. Guina, "High-efficiency 20 W yellow VECSEL," *Opt. Express* **22**, 6372–6380 (2014).